

Optimisation of current injection protocol based on a region of interest

This content has been downloaded from IOPscience. Please scroll down to see the full text.

2017 Physiol. Meas. 38 1158

(<http://iopscience.iop.org/0967-3334/38/6/1158>)

View [the table of contents for this issue](#), or go to the [journal homepage](#) for more

Download details:

IP Address: 128.41.61.19

This content was downloaded on 02/06/2017 at 15:28

Please note that [terms and conditions apply](#).

You may also be interested in:

[Correcting electrode modelling errors in EIT on realistic 3D head models](#)

Markus Jehl, James Avery, Emma Malone et al.

[Are patient specific meshes required for EIT head imaging?](#)

Markus Jehl, Kirill Aristovich, Mayo Faulkner et al.

[An electrode addressing protocol for imaging brain function with electrical impedance tomography](#)

L Fabrizi, A McEwan, T Oh et al.

[Correction of electrode modelling errors in multi-frequency EIT imaging](#)

Markus Jehl and David Holder

[Modelling for imaging neuronal depolarization by electrical and magnetic detection impedance tomography](#)

O Gilad, L Horesh and D S Holder

[In vivo bioimpedance changes during haemorrhagic and ischaemic stroke in rats: towards 3D stroke imaging using electrical impedance tomography](#)

T Dorrack, C Blochet and D Holder

[A comparison of two EIT systems suitable for imaging impedance changes in epilepsy](#)

L Fabrizi, A McEwan, T Oh et al.

[A method for reconstructing tomographic images of evoked neural activity with electrical impedance tomography using intracranial planar arrays](#)

Kirill Y Aristovich, Gustavo Sato dos Santos, Brett C Packham et al.

Optimisation of current injection protocol based on a region of interest

Mayo Faulkner¹, Markus Jehl, Kirill Aristovich, James Avery, Anna Witkowska-Wrobel and David Holder

University College London, London WC1E 6BT, United Kingdom

E-mail: mayo.faulkner@ucl.ac.uk

Received 12 December 2016, revised 24 March 2017

Accepted for publication 29 March 2017

Published 22 May 2017



CrossMark

Abstract

Objective. Electrical impedance tomography has the potential to image fast neural activity associated with physiological or epileptic activity throughout the brain. These applications pose a particular challenge as expected voltage changes on the electrodes are less than 1% and geometrical constraints of the body under investigation mean that electrodes can not be evenly distributed around its boundary. Unlike other applications, however, information regarding the location of expected activity is typically available. An informative method for choosing current paths that maximise sensitivity to specific regions is desirable. *Approach.* Two electrode addressing protocol generation methods based on current density vectors concentrated in a region of interest have been proposed. One focuses solely on maximising its magnitude while the other considers its distribution. The quality of reconstructed images using these protocols was assessed in a simulation study conducted in a human and rat mesh and compared to the protocol that maximises distance between injecting electrodes. *Main results.* When implementing the protocol that focused on maximising magnitude, the current density concentrated in a region of interest increased by up to a factor of 3. When the distribution of the current was maximised, the spread of current density vectors increased by up to fivefold. For the small conductivity changes expected in the applications explored, image quality was best when implementing the protocol that maximised current density. The average image error when using this protocol was 7% better than when employing other protocols. *Significance.* We conclude that for fast neural EIT applications, the protocol that maximises current density is the best protocol to implement.

¹ Author to whom any correspondence should be addressed.



Original content from this work may be used under the terms of the [Creative Commons Attribution 3.0 licence](https://creativecommons.org/licenses/by/3.0/). Any further distribution of this work must maintain attribution to the author(s) and the title of the work, journal citation and DOI.

Keywords: electrical impedance tomography, current injection protocol, fast neural EIT, epilepsy

(Some figures may appear in colour only in the online journal)

1. Introduction

1.1. Background

Electrical impedance tomography is a three-dimensional imaging technique in which the conductivity distribution within a volume can be reconstructed from voltage measurements on its boundary (Metherall *et al* 1996). The current injection protocol describes the set of electrodes through which current is sequentially injected, the choice of which greatly influences the sensitivity to perturbations in different locations. Approaches to optimise the current injection protocol have included those based on distinguishability (Isaacson 1986, Adler *et al* 2011) as well as more application specific methods. These include breast (Dehghani *et al* 2005), head (Fabrizi *et al* 2009) and cardiac (Tehrani *et al* 2012) EIT. While, in theory, methods such as that proposed by Adler *et al* (2011) can be applied to generalised domains, the emphasis has been on applications where concentric rings of external electrodes are placed in 2D or quasi-2D configurations and sensitivity to the whole volume is desirable (Adler *et al* 2011, Mamtjan *et al* 2012). For 3D domains, Malone *et al* (2014b) have proposed using a protocol that maximises the distance between injecting electrodes to enhance sensitivity to perturbations throughout the volume.

EIT can image fast neural activity occurring in the cortex with a spatial and temporal resolution of 200 μm and 2 ms (Aristovich *et al* 2016). Modelling has shown that it has the potential to record activity concurrently occurring in deep structures (Aristovich *et al* 2014, 2016). This has, however, yet to be realised in experiments (Vongerichten 2014). It is an application where the area of activity expected can be predicted beforehand given a known physiological stimulus and is conducted with internal electrodes that are limited to surgically accessible areas, typically the surface of the cortex. In order to realise the potential of EIT to image throughout the brain, maximising current reaching pertinent deep structures would be crucial. Fast neural EIT would benefit from the development of a dedicated protocol generation method that concentrates current into regions of interest (ROI).

The proposed use of EIT in improving the localisation of epileptic foci is another envisaged application which would profit from the development of such a protocol. The current proposition is for EIT to be used with preimplanted depth electrodes to locate the positions of the epileptic onset more accurately in patients that require resective surgery (Witkowska-Wrobel *et al* 2016). The advantage of using EIT is that it is sensitive to activity regardless of the orientation of the source (Ebersol 1997), and if external scalp electrodes are additionally implemented then activity occurring outside the vicinity of the depth electrode coverage can also be detected. As with fast neural EIT, electrodes are placed internally in irregular configurations and a target region in the volume can be specified.

1.2. Purpose

The purpose of this work was to develop an optimal electrode addressing protocol for EIT applications where a ROI can be specified and a non-concentric arrangement of electrodes are implemented. Rather than develop a protocol with uniform sensitivity throughout the volume, two protocols schemes that intend to maximise sensitivity to a predefined ROI were developed.

The first maximised the current density in the ROI. The second intended to maximise the magnitude and spread in the ROI, with the premise that it is desirable to probe the ROI from as many angles as possible in order to accurately locate it. The questions to be answered were,

- (i) Is the intended objective of the protocol achieved?
- (ii) Which protocol produced the best image quality?

1.3. Experimental design

The models to explore were chosen from two realistic applications, detecting epilepsy in the human head and recording fast neural activity in the rat brain. The human example was derived from a subject with frontal lobe epilepsy who had had depth electrodes inserted for presurgical evaluation. Scalp electrodes were also added in order to be sensitive to a larger region of the brain. The aim was to find the best protocol for detecting seizure activity. For this case, eight ROIs throughout the white and grey matter were simulated. Five of these were placed near the frontal lobe depth electrodes to reflect estimated sites for the origin of the seizure. The remaining three were added in the contralateral hemisphere.

The rat model considered was related to current studies in which fast neural impedance changes are recorded using an array of electrodes placed on the surface of the cortex in an anaesthetised rat. The aim here was to find the best protocol to detect deep fast neural activity. In this model, four ROIs were considered. These included the ventral posterolateral (VPL) and dorsal lateral geniculate (DLG) thalamic nuclei. These nuclei lie ventral to the cortex and are involved in somatosensory and visual processing respectively and would be ideal target structures from which to measure deep fast neural activity. Two ROIs were additionally placed in the cortex to assess the performance over a larger region of the brain.

In the human case, we propose that clinical use would be with a mixture of depth and scalp electrodes. In the rat case, we use only epicortical electrodes in order to increase SNR (Oh *et al* 2011). Therefore the simulations have mirrored this intended use. The human model employs depth and scalp electrodes and includes the CSF, skull and scalp, whereas the rat case only concerned the brain and epicortical electrode arrays and so the skull and scalp were removed from this model.

The current density vector concentrated in each ROI was determined for every possible injection pair. Using these values the two new protocols were established individually for each ROI. The first, the max J protocol, maximised the current density in the ROI. The second, the max A protocol, considered both the direction and the magnitude of the current density in each ROI.

The validity of the max J and max A protocols was assessed in a simulation study in which the quality of reconstructed images was used as a measure of performance. In both cases, their performance was compared to a protocol that is sensitive to the whole volume. This was chosen as the protocol that maximises the distance between injecting electrodes, the max D protocol (Malone *et al* 2014b).

In the rat case an additional protocol was also considered. This was the heuristic protocol previously implemented by Vongerichten (2014) in their study to image deep fast neural activity. It aimed to maximise sensitivity occurring in deep regions of the rat brain by injecting between the lateral most electrodes on opposite hemispheres.

As the envisaged applications for this study were locating epileptic foci and detecting fast neural activity in the human and rat case respectively, simulated perturbations in each ROI were representative of values expected in these applications (Fabrizi *et al* 2006, 2009, Oh *et al* 2011, Liston *et al* 2012). In order, however, to gain a broader understanding of the suitability of each protocol to different applications, larger conductivity changes were also investigated.

The two proposed protocols rely on accurate knowledge of the electrode positions with respect to the ROI. Errors between the simulated electrode positions used to generate the protocols and the experimental placement are inevitable and so the sensitivity of these protocols to electrode position errors has been investigated.

2. Methods

2.1. Mesh creation

3D anatomically accurate meshes of the rat brain and human head were created from CT and MRI scans of the respective subjects. A detailed description of the mesh generation pipeline and open source software required for this procedure is given in Jehl *et al* (2016). Briefly, Seg3D (CIBC 2016) was used to segment out layers of interest from the MRI and CT images. For the human head, six layers were identified; scalp, skull, white matter, grey matter, air and CSF. An additional layer containing the location of the depth electrode contacts within the subject was also extracted from the CT scan (Witkowska-Wrobel *et al* 2016). For the rat brain, three layers, white matter, grey matter and CSF were segmented. A high quality 3D mesh generator (The CGAL Project 2016) was then used to create tetrahedral meshes from these segmentations (Aristovich *et al* 2014, Jehl *et al* 2016). On the human head mesh, thirty-two scalp electrodes of 1 cm diameter were placed in positions defined by the EEG 10–10 configuration (Nuwer *et al* 1998, Jehl *et al* 2016) and twenty 1.1 mm diameter depth electrode contacts arranged on three probes were placed within the brain. The location of these contacts was found from the information in the additional layer extracted in the human CT scan. For the rat mesh, the location of electrodes was based on the position of arrays used in fast neural experiments attempting to detect deep activity (Vongerichten 2014); two electrode arrays containing fifty-seven 0.6 mm diameter electrodes were placed on each hemisphere of the mesh. The resulting human head and rat brain meshes comprised roughly 3 million tetrahedral elements of size 3 mm and 0.15 mm respectively, with elements refined to 0.8 mm and 0.06 mm in the vicinity of electrode contacts (Aristovich *et al* 2014).

2.2. Regions of interest

For the human head each ROI comprised all elements within the white and grey matter layers of the mesh whose centre lay within 1.5 cm of the specified position. ROI 1 and 2 were placed such that they lay between two depth electrode probes, figure 1(a). The remaining six ROIs were positioned between a single depth probe and the external scalp electrodes. The mean distance between the depth contacts and each of the ROIs was between 54–85 mm, table 1. The nasion (marked as X in figure 1(a)) has been used as the reference to calculate the position of each ROI, table 1.

In the rat, the ROIs were the VPL and the cortical forepaw area (FP) in the left hemisphere of the brain and the DLG and the cortical whisker area (W) in the right hemisphere, figure 1(b). Their position, size and shape within the rat mesh were informed by the prior construction of a 3D atlas of brain structures using coronal brain slices taken from the Paxinos and Watson rat atlas (Paxinos and Watson 2013). The anterior most part of the cerebral cortex (marked as X in figure 1(b)) has been used as the reference to calculate the position of each ROI, table 2.

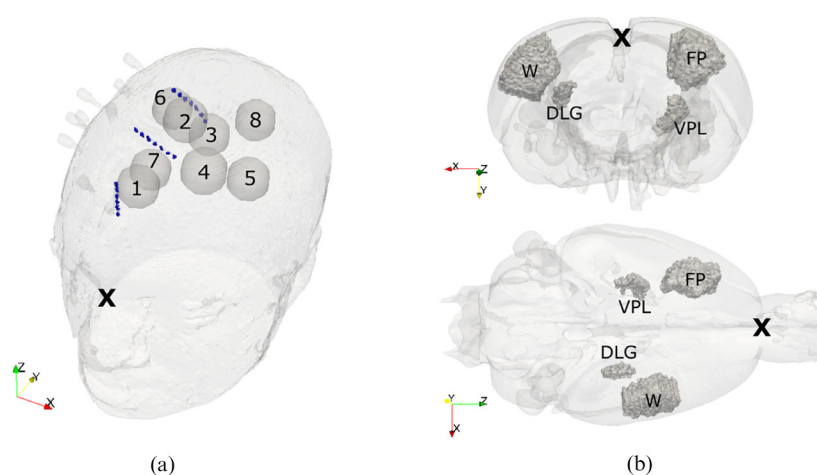


Figure 1. Location of regions of interest in (a) human mesh and (b) rat mesh. The location of the three depth electrode probes and their contacts can be seen dark blue in (a).

Table 1. Position of each ROI relative to the nasion (marked as X in figure 1(a)) in the human case. The fourth column indicates the mean distance of each ROI from the depth electrode probes.

ROI	Pos (mm)			Mean distance (mm)
	x	y	z	
1	-28	100	54	40
2	-8	130	94	36
3	-8	160	64	54
4	22	100	84	57
5	32	140	54	70
6	-43	170	69	64
7	-38	130	44	51
8	12	190	64	85

Table 2. Position of each ROI relative to the most anterior part of the cerebral cortex (marked as X in figure 1(b)) in the rat case.

ROI	Pos (mm)		
	x	y	z
VPL	3.1	-4.5	8.6
DLG	-3.4	-3.2	10.2
FP	3.7	-0.8	6.4
W	-5.0	-1.3	7.8

2.3. Current density calculation

The potential distribution in the mesh was simulated using the UCL SuperSolver Package (Horesh 2006). The tissue conductivities were assumed to be uniform and isotropic and were set to values compiled from literature for frequencies around 10 kHz, table 3 (Horesh

Table 3. Values of tissue conductivities compiled from literature by Horesh (2006) and used in simulations.

Tissue type	Conductivity (Sm^{-1})
White matter	0.15
Grey matter	0.3
CSF	1.79
Air	0.0001
Skull	0.018
Scalp	0.44

2006, Romsauerova *et al* 2006). In the human case the current was $50 \mu\text{A}$ unless the injection was between two scalp electrodes, in which case it was increased to $250 \mu\text{A}$. In the rat, the current injected was $50 \mu\text{A}$ between all pairs. The contact impedance on all electrodes was $1 \text{ k}\Omega$. The potential distribution was computed for current injected between one fixed electrode and all other electrodes. The remaining voltage distributions in the mesh for all other electrode pairs were calculated by subtracting one distribution from another, for example $V_{56-34} = V_{56-1} - V_{34-1}$. The current density within each element was calculated by finding the potential gradient across the element and multiplying by the conductivity within it.

2.4. Protocol generation

2.4.1. Max J protocol. The magnitude of the current density vector was found in each element by computing the 2-norm. By summing the magnitude across all elements in the ROI and dividing by the number of elements within it, a value for the average current density concentrated within the ROI was obtained. This value was established for every possible injection pair and the optimal protocol found by applying a maximum spanning tree weighted by these values.

A spanning tree of a graph finds the subgraph that connects all vertices using the minimum possible number of edges. In the resulting spanning tree only one possible path between any two vertices exists. A weighted graph is one where each edge has a value assigned to it. Among all the possible spanning trees of this weighted graph, the one with the largest total weight is called the maximum spanning tree. In the case considered here, the electrodes represent the vertices in the graph and an injection between a pair of electrodes the edge. The weight assigned to each edge is the current density concentrated in the ROI for that injection pair. The maximum spanning tree finds the independent protocol that addresses all electrodes while maximising the total current density in the ROI.

2.4.2. Max A protocol. This method was formulated on the principle that, in order to probe all directions, current density vectors must span the surface of a hemisphere. As the EIT current is alternating, it follows that the current density vectors in the other hemisphere are automatically explored.

The average x , y and z current density components of all elements in the ROI for every possible injection pair were calculated. For all injection pairs with a negative x current density component, the vector was translated into the opposite hemisphere. Vectors were then converted into spherical polar coordinates. The surface of the hemisphere was separated into six bins in both ϕ and θ giving a total of 36 bins into which the current density vectors of each injection pair were sorted.

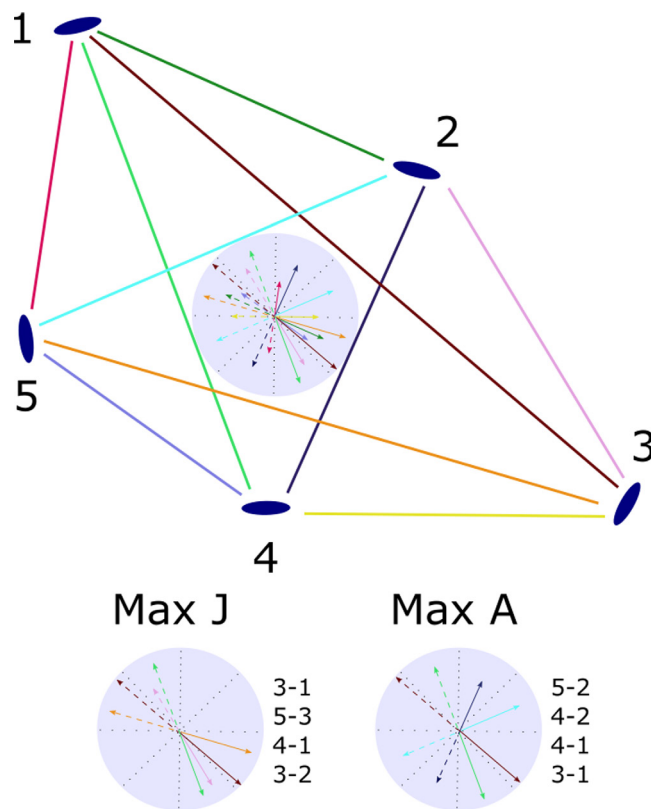


Figure 2. 2D conceptual diagram of protocols chosen using the proposed max J and max A protocols. The top diagram shows all possible injection pairs between five electrodes. The purple circle represents a ROI and the current density vectors resulting from all injection pairs are shown within it. The length of the current density vectors are representative of their magnitude. The dashed lines are to indicate that the current flow is alternating. The bottom left diagram shows the protocol chosen when using the max J approach. The independent injection pairs with the largest current density magnitude are chosen. The bottom right diagram shows the protocol chosen with the max A approach. The largest current density vector in each bin (represented by black dotted lines in this figure) is chosen.

The protocol was chosen using the following approach:

- (i) Sort bins in order of number of available injection pairs
- (ii) Choose pair with largest current density magnitude in each bin, starting from bin with the fewest available options
- (iii) If an electrode has been used twice, remove all combinations involving this electrode from other bins
- (iv) Once a single pair from each bin has been chosen, sort bins in order of current density magnitude of chosen injection pair
- (v) Choose additional injection pairs from bin with the lowest current density magnitude
- (vi) Continue until $N - 1$ injection pairs have been chosen

A diagram showing the approach used to identify the max J and max A protocols is given in figure 2.

2.4.3. Max D and heuristic protocols. The max D protocol was found by applying a maximum spanning tree weighted by the distance between electrodes (Malone *et al* 2014b). The heuristic (H) protocol was an ad hoc protocol implemented by Vongerichten (2014).

2.5. Voltage simulation and jacobian calculation

Electrode voltages and the Jacobian matrix were calculated using the PEITS forward solver (Jehl *et al* 2015b) and tissue conductivities, current amplitude and contact impedance values were the same as those used in section 2.3. In the human mesh all measurements on non-injecting electrodes were made with respect to a reference electrode placed on the nasion. This resulted in 50 measurements for each injection pair. For the rat mesh, measurements were obtained with respect to a reference electrode placed over the cerebellum area of the brain, yielding 112 measurements per injection pair.

Within each ROI, a spherical perturbation was simulated. The perturbations in the head mesh had a radius of 7 mm, and conductivity changes of 10%, 50% and 100% were modelled. A perturbation of radius 0.6 mm was placed in each ROI in the rat mesh and conductivity changes of 1%, 10% and 50% were simulated. Additive noise of 1 μ V, typical of the level expected in fast neural EIT applications, was added to all measurements.

2.6. Reconstruction

Zeroth order Tikhonov regularisation with noise based scaling was used to reconstruct images (Aristovich *et al* 2014). The regularisation parameter was chosen through generalised cross validation. Images were reconstructed on coarse meshes containing 1 million and 80 000 hexahedral elements of 3.5 mm and 0.3 mm in the human and rat brain respectively.

2.7. Quantification

2.7.1. Average current density. The average current density per protocol line (J) was used to quantify the amount of current concentrated in each ROI. This was calculated by summing the current density in the ROI for each injection pair in the protocol and dividing by the number of protocol lines.

2.7.2. Distribution of current density. The distribution of the current density was assessed by evaluating how uniformly spread the total current density was across the surface of a hemisphere. To examine this, the current density vector for each protocol line was converted into spherical polar coordinates and placed into its corresponding bin in the hemisphere. A metric to assess the uniformity of the distribution, the spread (*S*), was defined as,

$$S = \left(\frac{1}{J_T} \sum_{b=1}^{n_b} \left| j_b - \frac{J_T}{n_b} \right| \right)^{-1} \quad (1)$$

where J_T is the total current density concentrated in the ROI, n_b is the number of bins and j_b is the total current density in a single bin. A large *S* value corresponds to an uniform distribution of current density vectors.

2.7.3. Effect of electrode position errors. To investigate the sensitivity of each protocol to electrode position errors, the current density vector in each ROI (see section 2.3) was computed after having shifted the position of the electrodes. The resulting J and S values were

then computed for two cases. The first case used the current density vectors for the shifted electrode positions but implemented the optimised protocol for the original electrode position (original protocol). The second case computed these values when using the optimised protocol for the shifted electrode positions (shifted protocol). A one-way ANOVA was performed to identify if a significant difference between J and S values could be observed.

In the human case the scalp electrodes were shifted individually along each of the x , y and z direction with the direction of movement along each axis chosen randomly. For the depth electrodes, each of the three probes was similarly shifted in a random direction along each of the x , y and z axis. Three levels of electrode position error were considered: (1) 2 mm (Scalp) and 1 mm (Depth), (2) 5 mm and 2 mm and (3) 10 mm and 4 mm.

In the rat case the two arrays (each containing 57 electrodes) have been shifted in x and y , with the direction of shift being randomly assigned. All the electrodes on a single array have been moved in the same direction as they are physically constrained with respect to one another. Three levels of position error were considered: 0.6 mm, 1.2 mm and 1.8 mm.

2.74. Image quantification. The quality of reconstructed images was objectively evaluated using three error metrics (Packham *et al* 2012, Malone *et al* 2014b). For this analysis the volume corresponding to the reconstructed perturbation was defined as the largest connected cluster of voxels with at least 75% of the maximum absolute reconstructed change (Jehl *et al* 2015a). All error metrics are calculated with respect to an 'ideal' reconstructed image. The three metrics considered were defined as follows:

- Localisation error: the displacement of reconstructed centre of mass compared to the ideal centre of mass, expressed as a percentage of the average dimension of the mesh.
- Shape error: the mean of the difference in each axis of the reconstructed perturbation to the perturbation's actual width, expressed as a percentage of the mesh's dimensions.
- Image noise: the standard deviation of all conductivity changes not belonging to the reconstructed perturbation expressed as a percentage of the mean conductivity change in the reconstructed perturbation.

The total image error is defined as the sum of the three individual error metrics.

3. Results

3.1. Magnitude and spread of current density in ROI

The max J protocol concentrated the largest amount of current density into the ROI for all positions considered in both the human and rat case. When implementing this protocol in the human head, the current density concentrated in the ROI was between 1.5 and 3.2 times larger than when using the max A protocol and between 1.3 and 2.5 times greater than when using the max D protocol, table 4. In the rat, the max J protocol concentrated between 2.6 and 3.3 times more current than the max A protocol, between 1.3 and 2.9 times more than the max D protocol, and between 1.8 and 3 times more than the heuristic protocol, table 5. With the exception of position 6 in the human case, the max A protocol concentrated the least current into all ROIs. A one-way ANOVA was performed and showed a significant difference in J values between the protocols in the human case ($p < 0.01$). In the rat case, however, a significant difference between protocols was not observed.

The large S values observed with the max A protocol indicate that this protocol distributed the current density most evenly, tables 4 and 5. Apart from positions 3 and 5 in the human, the max J protocol resulted in the least variation in current density directions. A

Table 4. Current density (J) ($\text{mA}\cdot\text{m}^{-2}$) and spread (S) in the eight ROIs considered in the human mesh for the max A, max D and max J protocols.

		Pos 1	Pos 2	Pos 3	Pos 4	Pos 5	Pos 6	Pos 7	Pos 8	Mean
Max A	J	5.78	7.86	5.62	6.10	4.76	6.27	4.12	6.46	5.87
	S	2.15	3.04	2.78	2.26	2.17	2.64	3.18	2.42	2.58
Max D	J	7.55	8.18	6.07	6.80	6.06	6.22	5.71	6.58	6.65
	S	1.05	1.46	1.28	0.98	0.94	1.10	1.03	1.01	1.11
Max J	J	18.7	16.8	8.21	13.6	8.85	12.9	8.29	11.3	12.3
	S	0.56	0.72	1.44	0.64	0.96	0.79	0.84	0.71	0.83

Table 5. Current density (J) ($\text{A}\cdot\text{m}^{-2}$) and spread (S) in the four ROIs considered in the rat mesh for the max A, max D, max J and heuristic protocols.

		VPL	DLG	FP	W	Mean
Max A	J	0.15	0.19	0.68	0.71	0.43
	S	3.31	4.12	3.47	3.35	3.56
Max D	J	0.31	0.41	0.82	0.82	0.59
	S	0.75	0.82	1.19	1.14	0.98
Max J	J	0.39	0.56	2.16	2.34	1.36
	S	0.68	0.64	0.64	0.69	0.66
Heuristic	J	0.22	0.23	0.72	0.98	0.54
	S	0.75	0.80	0.91	0.68	0.79

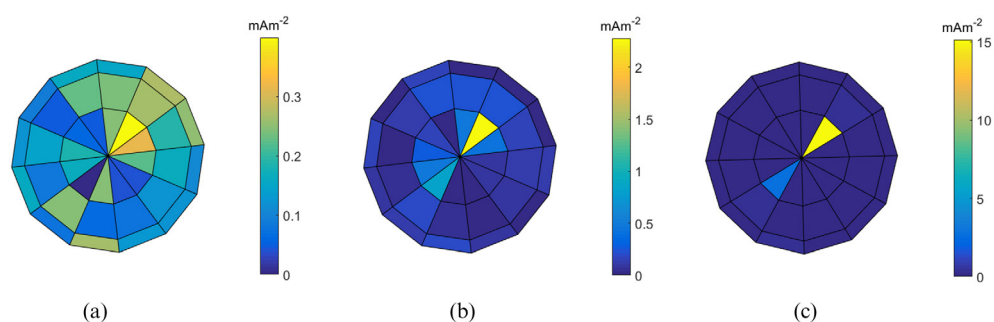


Figure 3. Heat map of current density concentrated within each bin on surface of a hemisphere for the max A, max D and max J protocols in position 1 in the human case. There is large variation in the scales between the three protocols with the max A protocol ranging from 0–0.4 $\text{mA}\cdot\text{m}^{-2}$, the max D from 0–2.3 $\text{mA}\cdot\text{m}^{-2}$ and the max J from 0–15 $\text{mA}\cdot\text{m}^{-2}$. (a) max A protocol. (b) max D protocol. (c) max J protocol.

significant difference in S values between protocols was observed in both the human and rat case ($p < 0.01$). An illustration of the difference in distribution of the current density across angles at position 1 in the human is shown in figure 3. In this example, the max J protocol resulted in only four non zero bins with the majority of the current density being concentrated within a single bin. On the other hand, when implementing the max A protocol, all except one bin contained current density vectors with little variation in values across bins.

3.2. Effect of electrode position error on protocols

In the human case, no significant difference ($p < 0.01$) was observed in J values between the original and shifted max A, max D and max J protocols for all three of the electrode position

Table 6. Protocol that resulted in the lowest image error for each ROI in the human case for the three conductivity changes considered.

	Pos 1	Pos 2	Pos 3	Pos 4	Pos 5	Pos 6	Pos 7	Pos 8
10%	J	J	A	J	J	J	J	J
50%	A	J	A	J	J	J	J	J
100%	A	A	A	J	J	J	J	J

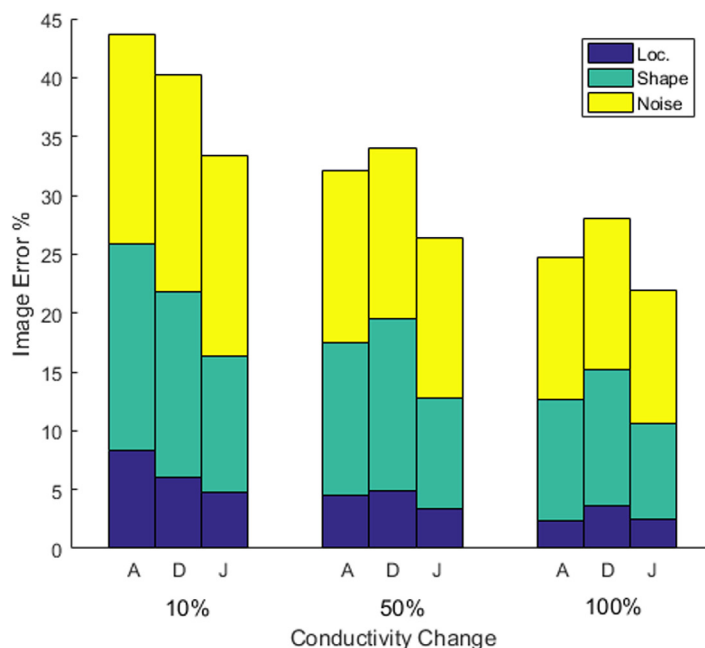


Figure 4. Total average image error for 10%, 50% and 100% conductivity changes across 8 ROIs in the human head. The first column in each group corresponds to the max A protocol, the second the max D protocol and the third the max J protocol.

errors considered. No significant difference in S values were found when implementing the original and shifted max D and max J protocols for any of the position errors. However, a significant difference in S values was observed between the original and shifted max A protocol for all variations of electrode errors. When comparing the S values obtained using the original max A, max D and max J protocols, a significant difference was present between these three protocols for all position errors considered.

In the rat, no significance was found between the J and S values computed when using the original and shifted max A, max D, max J and heuristic protocols for all of the three electrode position errors considered.

3.3. Impact of protocol on image error

3.3.1. Human case. For a 10% perturbation the max J protocol resulted in the reconstructions with the lowest image error in all positions apart from in position 3. In this position it was the max A protocol that yielded the lowest image error, table 6. The total and individual average image errors across the eight ROIs were smallest when using the max J protocol, figures 4 and 5. The max A protocol resulted in the highest localisation, shape and total average image error.

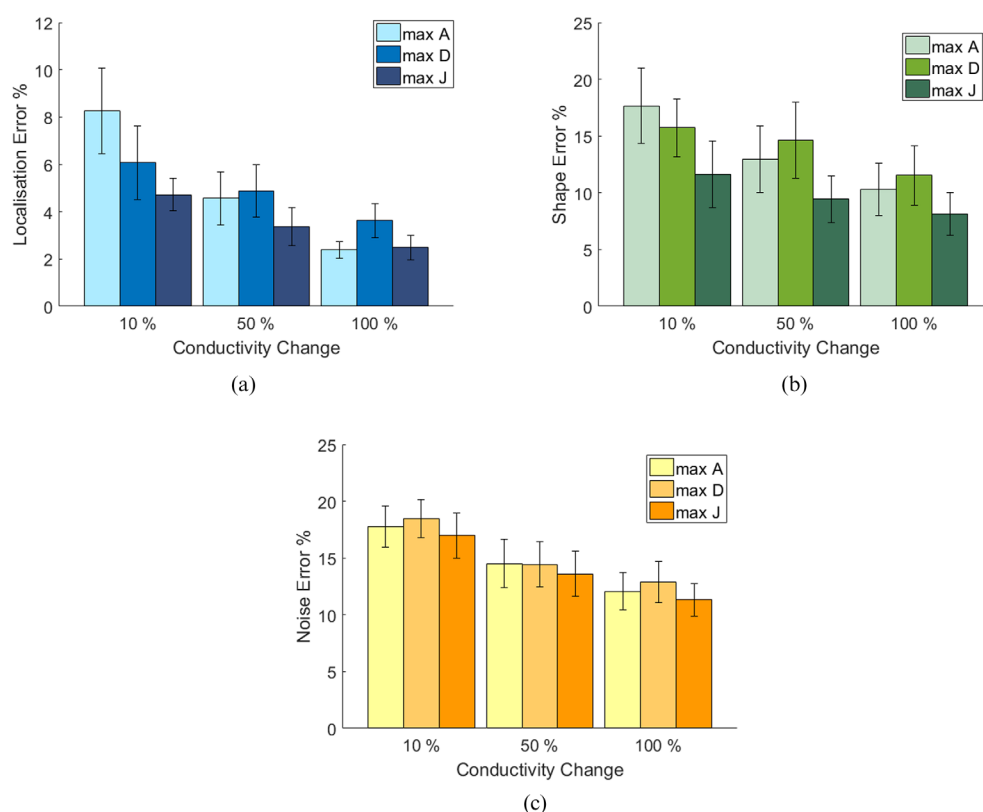


Figure 5. Individual average image errors for 10%, 50% and 100% conductivity changes across 8 ROIs in the human head (mean \pm S.E.). (a) Localisation error. (b) Shape error. (c) Noise error.

As the conductivity change was increased to 50%, once again in position 3 the max A protocol resulted in the lowest image error and this can be observed in the reconstructed images in figure 6. In position 1, the max A protocol also gave the lowest image error. In all other positions the max J protocol had the lowest image error, table 6. When averaged across the 8 ROIs the max A protocol yielded lower localisation, shape and total image errors when compared to the max D protocol. On average the max J protocol still resulted in the lowest image error, figures 4 and 5.

When a 100% conductivity change was simulated, in positions 1, 2 and 3, the max A protocol had the lowest image error. However, for the reconstructions in positions 1 and 2 all three protocols reconstructed images with very low errors and the difference in image error between the best and worst protocols was 0.8% and 0.7% in positions 1 and 2 respectively. In all other positions the max J protocol resulted in the lowest image error. On average, the trend in protocol performance follows that observed for the 50% case. The difference in the total average image error between the max A and max J protocols, however, becomes less distinct with increasing conductivity change.

The influence of the position of the perturbation with respect to the depth electrodes is apparent in figure 6. The perturbations in positions 1 and 2 had the closest average distance from the depth electrode contacts, table 1, and were most accurately reconstructed with all three protocols.

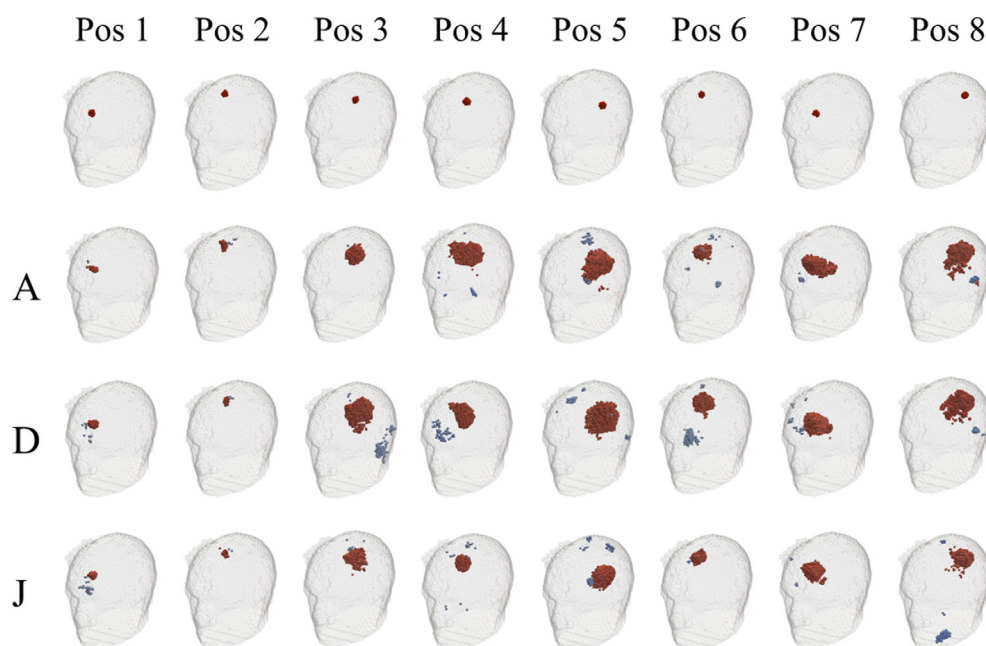


Figure 6. Reconstruction for 50% conductivity change in all eight ROIs in human head for three different protocols. All images have been thresholded at 75% of the maximum reconstructed change. Top row shows the ideal reconstructed image.

3.3.2. *Rat mesh.* For a 1% conductivity change the max J protocol resulted in the lowest image error in all ROIs apart from W. In this ROI, the max A protocol had the lowest image error, table 7. When averaged across the four ROIs, the max J protocol yielded the lowest image error, despite the average localisation error being larger than that of the max D protocol. The max J protocol was followed by the max D protocol and then the max A protocol, figure 7. On average, the heuristic protocol resulted in the highest image error even though it concentrated more current into the ROIs than the max A protocol. This can be attributed to the large average shape error observed when using this protocol, figure 8.

When the conductivity change was increased to 10% the max J protocol yielded the lowest image error in the VPL and the DLG. In the two cortical ROIs, FP and W, the max A protocol had the lowest image error. The difference in quality of reconstruction between the protocols was much more significant in the VPL and DLG when compared to the cortical ROIs and this can be observed in the reconstructions in figure 9. On average, the max J protocol resulted in the reconstructions with the lowest image errors, followed by the max A protocol and then the max D protocol. Once again the heuristic protocol had the highest average image error.

For a 50% conductivity change, the max A protocol had the lowest image error in all four ROIs considered, table 7. On average, the max A protocol had the lowest total, localisation, shape and noise errors; this was followed by the max J protocol. The heuristic protocol had a slightly lower average image error than the max D protocol.

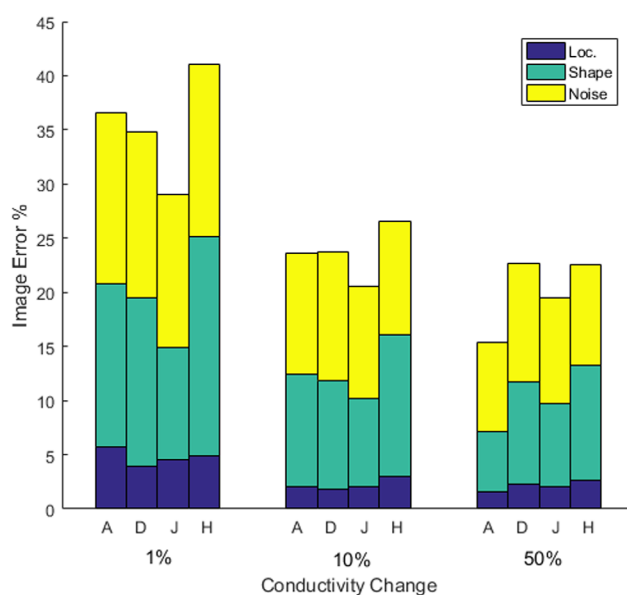


Figure 7. Total average image error for 1%, 10% and 50% conductivity changes across 4 ROIs in the rat. The first column in each group corresponds to the max A protocol, the second the max D protocol, the third the max J protocol and the fourth the heuristic (H) protocol.

Table 7. Protocol that resulted in the lowest image error for each ROI in the rat case for the three conductivity changes considered.

	VPL	DLG	FP	W
1%	J	J	J	A
10%	J	J	A	A
50%	A	A	A	A

4. Discussion

4.1. Protocols

At the outset the aim of the max J protocol was to find a set of independent current injection pairs that maximise the current density concentrated in a ROI. In the human there was a significant difference in average J value across ROIs between protocols. In the rat, however, a significant difference was not observed. This lack of significance is likely due to large variation in J values between the two deep ROIs, the VPL and VPM, and the two cortical ROIs, FP and W, tables 4 and 5. For all positions in both mediums considered, the protocol generated using this method yielded the largest average current density.

The goal of the max A protocol was to have current density vectors passing through the ROI in as many directions as possible while also aiming to maximise the magnitude of the current density within it. For all positions the max A protocol resulted in the protocol where the current density was most evenly spread across the surface of a hemisphere, tables 4 and 5. This method aimed also to maximise the magnitude of the current density in the ROI; however, for seven out of eight positions in the human and in all positions in the rat, it resulted in the lowest current density magnitude. Therefore there is a clear trade off between maximising the spread and maximising

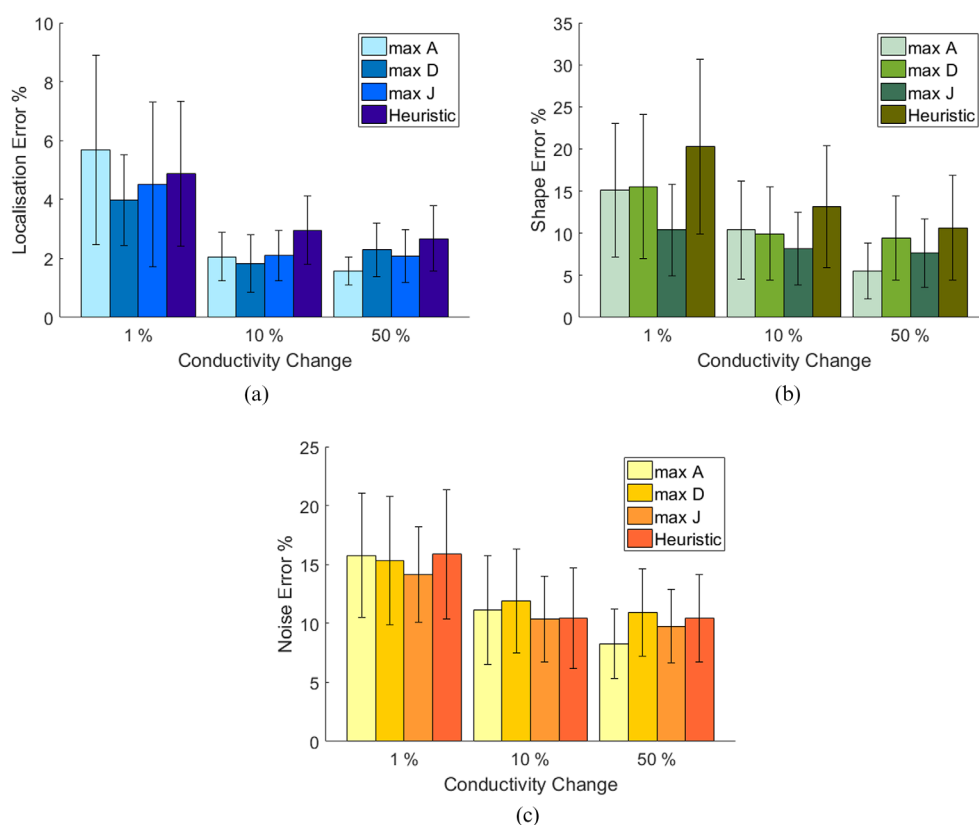


Figure 8. Individual average image errors for 1%, 10% and 50% conductivity changes across 4 ROIs in the rat (mean \pm S.E.). (a) Localisation error. (b) Shape error. (c) Noise error.

the current density magnitude. When generating this protocol, the iterative search method started by looking at bins containing the fewest current injection pairs. In this way the emphasis was on maximising the spread of current density. It would be possible to alter the search method and look for the largest pairs first. This would increase current density magnitude at the expense of spread.

The max J protocol was found not be sensitive to errors in electrode positions. Even with the largest shifts in electrode errors considered in both the human and rat case no significant difference in J values was observed between the optimised protocol based on the original electrode positions and the protocol optimised to the shifted electrode positions. This indicates that even if slight positional deviations are present between the electrodes used to generate the max J protocol and those used in experiments, the benefit of increased current density magnitude attributed to implementing the max J protocol is still observed.

A significant difference in S values was found between the original and shifted max A protocol in the human. This significance was not observed in the rat case. The high sensitivity to electrode position errors in the human case could be attributed to the presence of the depth electrodes which permit larger control over the current density vectors. A significant difference was observed when comparing the S values resulting from the original max A, max D and max J protocol for all electrode errors. Therefore, even though the increase in S values is not as large as when using the protocol optimised for the shifted electrode positions, the S values are still larger than those resulting from the max D and max J protocols.

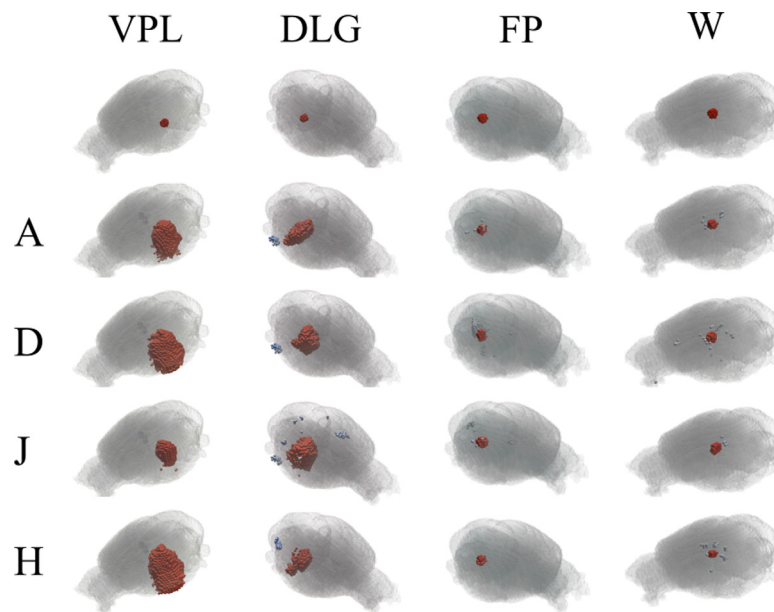


Figure 9. Reconstruction for 10% conductivity change in all four ROIs in rat for four different protocols. All images have been thresholded at 75% of the maximum reconstructed change. Top row shows the ideal reconstructed image.

4.2. Impact of protocol on image quality

When small conductivity changes were simulated, 10% in the human case and 1% in the rat case, the max J protocol reconstructed images with the lowest error. Generally, for these changes considered, image quality correlated with current density magnitude. Specifically the protocols that concentrated more current density in the ROI resulted in lower image errors. The only exception was in the rat where, despite the heuristic protocol concentrating more current into the ROI than the max A protocol, it resulted on average with a higher image error. For small changes, the indication is therefore that the influence of high current density magnitude outweighs any advantages that may be observed due to increased spread in current density. Interestingly in position 3 in the human case, even for the 10% conductivity change considered, the max A protocol resulted in the lowest image error. In this position the difference in current density magnitude between the max A and the max J protocol was the smallest out of all the ROIs considered. This suggests that ideally high spread and high current density is desirable.

For the 50% and 100% conductivity changes simulated in the human case and the 10% conductivity change in the rat case, on average the max J protocol still resulted in the lowest image error. It was, however, the max A protocol that now resulted in the second best image errors on average. For these changes it appears that compared to the max D and heuristic protocols, the increased spread observed with the max A protocol is advantageous. Even at these conductivity change levels, however, the increase in current density magnitude attained with the max J protocol is still beneficial over any increased spread that can be achieved with the max A protocol.

For a 50% conductivity change in the rat, the max A protocol outperformed the max J protocol in all ROIs. The indication is that for this level of conductivity change in the rat, there is no longer a benefit of having a high current density magnitude and indeed a protocol with larger variations in angles results in better reconstructed images. While on average the max J protocol

had a lower image error than the max A protocol for the 100% conductivity change in the human, for perturbations placed in the vicinity of the depth electrodes, positions 1 and 2, the max A protocol actually resulted in a lower image error than the max J protocol. Given this single instance, and the small variations in error between the protocols, however, it is not possible to conclude for this case whether the max A protocol would offer generalised improvements.

For epilepsy and fast neural activity, the primary applications for which this work has been conducted, the conductivity changes can not be expected to exceed 10% or 1% respectively. The recommendation therefore would be to use the max J protocol and this protocol is currently being implemented in clinical experiments involving epileptic patients with depth electrodes and in rat experiments to detect deep neural activity. For applications where larger changes can be anticipated, however, the choice of the max A protocol may be better suited for more accurate reconstructions. It must be reiterated that this is for specific cases where a predefined ROI can be identified.

5. Conclusion

Two protocol generation methods based on the magnitude and distribution of current density concentrated in a ROI have been developed. Their performance has been assessed based on the quality of reconstructed images and compared to previously implemented protocol in two mediums, a head and rat mesh. The results from the simulations suggest that, when the signal is small, increased current density magnitude attributed to implementing the max J protocol improves image quality. There is a suggestion that once the signal is large enough the advantage of using a protocol that maximises current density is diminished and instead it is beneficial to implement one that contains a spread of current directions. This was observed in the rat for a 50% conductivity change. In general the max A protocol did not improve image quality consistently enough to recommend using it over other protocol schemes. To fully establish if there is indeed an advantage of spreading current density vectors, the recommendation would be to repeat the study in other 3D domains with different configurations of electrodes. This work has used a simplified model where all tissues are assumed to be isotropic. In reality, the white matter, scalp and skull are known to be highly anisotropic (Abascal *et al* 2008). Further work could incorporate a forward solver that supports anisotropic conductivities and directly translate the presented methods to optimise the current injection protocol to this anisotropic model.

Acknowledgments

This work was supported by DARPA grant N66001-16-2-4066, Blackrock Microsystems and the EPSRC.

References

- Abascal J, Arridge S, Atkinson D, Horesh R, Fabrizi L, De Lucia M, Horesh L, Bayford R and Holder D 2008 Use of anisotropic modelling in electrical impedance tomography: description of method and preliminary assessment of utility in imaging brain function in the adult human head *NeuroImage* **43** 258–68
- Adler A, Gaggero P and Maimaitjiang Y 2011 Adjacent stimulation and measurement patterns considered harmful *Physiol. Meas.* **32** 731–44
- Aristovich K Y, Packham B C, Koo H, Sato Dos Santos G, McEvoy A and Holder D S 2016 Imaging fast electrical activity in the brain with electrical impedance tomography *NeuroImage* **124** 204–13
- Aristovich K, Sato Dos Santos G, Packham B and Holder D 2014 A method for reconstructing tomographic images of evoked neural activity with electrical impedance tomography using intracranial planar arrays *Physiol. Meas.* **35** 1095–109

- CIBC 2016 Seg3D: Volumetric Image Segmentation and Visualization (Scientific Computing and Imaging Institute (SCI)) <http://seg3d.org> (Accessed: 16 December 2015)
- Dehghani H, Soni N, Halter R, Hartov A and Paulsen D K 2005 Excitation patterns in three-dimensional electrical impedance tomography *Physiol. Meas.* **26** S185
- Ebersol J S 1997 Defining epileptogenic foci: past, present, future *J. Clin. Neurophysiol.* **14** 470–83
- Fabrizi L, McEwan A, Oh T, Woo E J and Holder D S 2009 An electrode addressing protocol for imaging brain function with electrical impedance tomography using a 16-channel semi-parallel system *Physiol. Meas.* **30** S85
- Fabrizi L, Sparkes M, Horesh L, Abascal J, McEwan A, Bayford R, Elwes R, Binnie C and Holder D 2006 Factors limiting the application of electrical impedance tomography for identification of regional conductivity changes using scalp electrodes during epileptic seizures in humans *Physiol. Meas.* **27** 163–74
- Horesh L 2006 Some novel approaches in modelling and image reconstruction for multi frequency electrical impedance tomography of the human brain *PhD Thesis* University College London
- Isaacson D 1986 Distinguishability of conductivities by electric current computed tomography *IEEE Trans. Med. Imaging* **5** 91–5
- Jehl M, Aristovich K, Faulkner M and Holder D S 2016 Are patient specific meshes required for EIT head imaging? *Physiol. Meas.* **37** 879
- Jehl M, Avery J, Malone E, Holder D and Betcke T 2015a Correcting electrode modelling errors in EIT on realistic 3D head models *Physiol. Meas.* **36** 2423–42
- Jehl M, Dedner A, Betcke T, Aristovich K, Klöforn R and Holder D 2015b A fast parallel solver for the forward problem in electrical impedance tomography *IEEE Trans. Biomed. Eng.* **62** 126–37
- Liston A, Bayford R and Holder D 2012 A cable theory based biophysical model of resistance change in crab peripheral nerve and human cerebral cortex during neuronal depolarisation: implications for electrical impedance tomography of fast neural activity in the brain *Med. Biol. Eng. Comput.* **50** 425–37
- Malone E, Jehl M, Arridge S, Betcke T and Holder D 2014b Stroke type differentiation using spectrally constrained multifrequency EIT: evaluation of feasibility in a realistic head model *Physiol. Meas.* **35** 1051–66
- Mamtjan Y, Ah S J, Oh T and Adler A 2012 Optimised electrode positions and stimulations patterns in head EIT *Canadian Medical and Biological Engineering Society (CMBEC 35)*
- Metherall P, Barber D C, Smallwood R H and Brown H 1996 Three-dimensional electrical impedance tomography *Nature* **380** 509–12
- Nuwer M, Comi G, Emerson R, Fuglsang-Frederiksen A, Guérit J M, Hinrichs H, Ikeda A, Luccas F and Rappelsburger P 1998 IFCN standards for digital recording of clinical EEG *Electroencephalogr. Clin. Neurophysiol.* **106** 259–61
- Oh T, Gilad O, Ghosh A, Schuettler M and Holder D S 2011 A novel method for recording neuronal depolarization with recording at 125–825 Hz: implications for imaging fast neural activity in the brain with electrical impedance tomography *Med. Biol. Eng. Comput.* **49** 593–604
- Packham B, Koo H, Romsauerova A, Ahn S, McEwan A, Jun S and Holder D 2012 Comparison of frequency difference reconstruction algorithms for the detection of acute stroke using EIT in a realistic head-shaped tank *Physiol. Meas.* **33** 767–86
- Paxinos G and Watson C 2013 *The Rat Brain in Stereotaxic Coordinates* 7th edn (Amsterdam: Elsevier)
- Romsauerova A, McEwan A, Horesh L, Yerworth R, Bayford R and Holder D 2006 Multi-frequency electrical impedance tomography (EIT) of the adult human head: initial findings in brain tumours, arteriovenous malformations and chronic stroke, development of an analysis method and calibration *Physiol. Meas.* **27** 147–61
- Tehrani J N, Oh T, Jin C, Thiagalingam A and McEwan A 2012 Evaluation of different stimulation and measurement patterns based on internal electrode: application in cardiac impedance tomography *Comput. Biol. Med.* **42** 1122–32
- The CGAL Project 2016 Computational Geometry Algorithms Library (CGAL Editorial Board) www.cgal.org (Accessed: 15 May 2017)
- Vongerichten A 2014 Imaging physiological and pathological activity in the brain using electrical impedance tomography *PhD Thesis* University College London
- Witkowska-Wrobel A, Aristovich K, Avery J and Holder D 2016 A method for imaging epilepsy with EIT and depth electrodes *Proc. of the 17th Int. Conf. on Biomedical Applications of Electrical Impedance Tomography* p 149